IAC-14-B4, 4.4.25291

Practical Strategies to Stabilize A Nanosatellite Platform with A Space Camera and Integrated Mechanical Parts

Junquan Li, Steve Greenland, Craig Clark
Clyde Space Ltd, United Kingdom,
junquan.li@clyde-space.com, Steve.Greenland@clyde-space.com, Craig.clark@clyde-space.com

Mark Post
Space Mechatronic Systems Technology Laboratory
Department of Design, Manufacture and Engineering Management University of Strathclyde, UK,
mark.post@strath.ac.uk

Andy Vick, David Pearson, David Lee, Donald MacLeod
UK Astronomy Technology Centre, United Kingdom,
Andy.Vick@stfc.ac.uk, David.pearson@stfc.ac.uk, David.lee@stfc.ac.uk, donald.macleod@stfc.ac.uk

The growth and speed of nanosatellite capabilities has lead to an increasing demand on the respective attitude control systems. Typically, nanosatellites utilize miniaturized reaction wheels for 3 axis stabilization and manoeuvres, which are desaturated using magnetorquers. Small space telescopes have been deployed from nanosatellites in the past with capability ever increasing to push the limit of detectors. Previous work has established the feasibility of achieving GSD of 0.7m in the low Earth orbit for a 2.5 U Cubesat using deployable mirrors from a 400km orbit. The dynamic model of a nanosatellite with the telescope and deployed mirror systems will be built in this research work. The deployed mirror system will use a diamond turned mirror for the initial prototype, it is an off axis paraboloid. The mirror would be light weighted as much as possible, i.e. the back surface would be carved with good thermal stability. The mechanisms for mirror systems may use methods like miniature geared motors, stiction motors and shape memory alloy hinges. The sensing and directing of the mirror surface will use an image based detection methods. A closed loop control of the mirror position will be used to iterate to a fully aligned system. This work also considers control strategies to stabilize such a platform against the effects of firstly, the external aerodynamics and secondly, any internal disturbances induced by and the movement of focusing elements. A pointing accuracy of less than one arcsec for a 10 min observation over the UK is targeted at a baseline orbit of 350km sun synchronous. Following an initial baseline to establish current state of art both based on in orbit performance and off the shelf subsystems available to the market within the constraints of a 3U nanosatellite system, a number of feed forward or feedback control loops and sensor systems are studied to determine a simple process for compensating for the motion.

I INTRODUCTION

The first Earth observing satellite $TIROS - 1$ was launched in 1960. Since 1960, hundreds of Earth observation satellites have been launched for Earth sciences, including climatology, aeronomy, atmospheric chemistry, oceanography, geology, biology, hydrology, and so on [1]. The miniaturization trend in spacecraft has been lead by Jordi Puig-suari at Cal Poly and Bob Twiggs at Stanford. Since 1999, a large number of cubesat programs have been developed with typical payloads such as GNSS receivers, CMOS or CCD cameras and space weather sensors [2]. In Reference [1], a few Earth observation Cubesat mission with advanced remote sensing payloads have been summarized. These nanosatellites with telescopes and cameras, such as a passive optical telescope with 188x120 pixel camera on SwissCube-1 at the Polytechnic School of Lausanne, a telescope with 1626x1236 pixel CCD 25.4 mm aperture, 17.6 mm focal length on Michigan Multipurpose minisatellite , a CMOS color camera with 640x480 pixel on ION at the University of Illinois at Urbana-champaign have been launched in the last ten years. PRISM with deployed telescope was launched by the University of Tokyo in 2009. This satellite is a 8.5kg nanosatellite with a 800 mm extensible boom and solar array paddles [3]. The CMOS camera was 102mm aperture with 1280x1024 pixels. This nanosatellite has 30m ground resolution at 550 km sun-synchronous orbit. The attitude determination and control system for PRISM was a three axis stabilized system used magnetometers, gyros, sun sensors for attitude sensors.

The magnetorquers were used for actuators. The use of one reaction wheel and the piezo motor for attenuating the vibration was used as a demonstration. ADCS was required for steering the lenses at Earth and steering in the desired direction using the sensors capturing the horizon of the Earth or the direction of the moon.

Several other nanosatellites and microsatellites were developed for optical payloads with low cost, low mass and small volume. One of the methods is to use deployable telescopes. They can maintain the capabilities of the classics telescope and have lighter weight and easy for small launch volume. FalconSat-7 by Air Force, is a 3U nanosatellite with a rigid boom structure that can support a membrane photon sieve flat to precise requirement [4]. It will take the image of the sun. It uses the photon sieve technology which is a novel optical element consisting of a flat opaque sheet with millions of tiny holes. The advantages of such design are lightweight and low fabrication costs. The disadvantages are lower efficiency, loss of light and narrow bandwidth. NASA Ames Research center has been investigating deployable optical collapsible Dobson telescopes on a small 6U Nanosatellite for commercial uses [5] . The strain deployable 152.3mm-154.2 f/8 or f/9 Ritchey Chretien telescope occupying a 4U bay with a wider aperture was compared to other solutions. Piezo electric tilt tip and z axis actuation of the secondary mirror have been used for the misalignment of optics. A Canon camera was connected to the telescope and images were taken remotely using an iPad over the network. The recent telescope nanosatellite work at the University of Tokyo is

"Nano-JASMINE" [6]. It is a 35 kg micro satellite with a 5 cm diameter telescope and a CCD with time delay integration (TDI). The satellite will be used to measure the positions of twenty thousands of stars in the sky. The ADCS design requirement includes the errors of angular rate less than $4e-7$. The star trackers, a fibre optical gyro, sun sensors, coarse magnetometer, precise magnetometer, four reaction wheels as well as three magnetic torquers have been used for the precise attitude control systems. Microsatellite were used as an earth observing platform. Surrey Satellite Technology have developed many optical systems for micro satellites less than 500 kg. The optical system has the capable of sub-1m ground sampling resolution. An SSTL-300 with TDI detectors could give a 1.5m ground resolution at the altitude of 400 km. Remote sensing customers are requiring resolutions down to 0.6 m even from relatively low cost small satellites. Some of the solutions are using the Three-Mirror Anastigmat (TMA) or Korsch, Newtonian camera design [7]. However, the manufacture and mounting sensitivities are not easy. In Reference [7], the authors points out that resolutions are not only camera design problems. The performance can be traded against orbit parameters (orbit altitude), the propulsion systems sizing for orbit maintenance, system mass, complexity, size, and delivery time.

A deployable small telescope prototype was designed at the UK Astronomy Technology Centre (UK ATC), United Kingdom. Some previous design includes the use of a 2.5 U Cubesat using deployable mirrors from a 400km orbit. In this research paper, we will discuss the system design of the deployable telescope with the 3U nanosatellite. The chosen MATLAB/SIMULINK software environment allows us to build an architecture permitting a rapid model development and ease of visualization. Many approaches will be adopted in this work, such as using light materials, the design of optimal structure and the fold-able telescope structure. The deployable primary mirrors and secondary mirrors will be released to restore its original shape after the launch phase. For the future use of halo orbit at L2, the prototype of this telescope will be demonstrated in the low Earth orbit. Satellite pointing system and attitude control system will be discussed in this research paper. The resolution of a deployable telescope for a 3U nanosatellite is about one tenth of what can be delivered by big satellites, but it is enough to identify individual objects on the ground. The primary objective of such demonstration will be 'Take a picture of a designated ground object of interest and have that image relayed back to the ground station during the satellite pass, within an approximately 10-20 min cycle'. The focused rays must be detected with a Charge-Coupled Device (CCD) and sufficient high bandwidth control and electronics for the images processing and transmitted back to the ground station.

In this research paper, first, the optical system of the Cassegrain telescope will be analyzed. The CCD detector will be selected. Second, The MEMS deformable structure of telescope with the primary and secondary mirrors will be discussed. Third, the design and simulation results of an attitude control system for this optical system will shown in this paper. The adjusting mechanism with piezoelectric actuators will be used in this work. Finally, the conclusion and future work will be discussed.

Name	Value
Telescope Focal Length	450mm
Distance Primary Secondary	200mm
Primary Mirror Diameter	300mm
Primary mirror Focal Leigh	210mm
Primary mirror conic coefficient	-1.0
Secondary Mirror Diameter	25mm
Secondary Mirror Focal Length	16mm
Secondary mirror conic coefficient	-1.23

Table 1. Telescope Characteristics

Name	Value
Date Rate	40 MHZ
Linear Resolution	2048x96
Max Line Rate	17 KHZ
Max Line Time	59 μ s
Pixel Size	13 μm x13 μm
Gain Range	-8.5 9.5 dB

Table 2. CCD Detector Characteristics

II OPTICAL DESIGN

There are three telescope designs that have been considered: refracting, Newtonian, and Cassegrain [8]. After the comparison of compressibility, complexity, mass distribution, image performance and thermal sensitivity, the Cassegrain telescope design is chosen. The UK ATC prototype telescope optical design consists of a two mirror Cassegrain telescope with a parabolic primary, a hyperbolic secondary, and field corrector lenses. This design is suited for the deployable optics due to its rotational symmetry and separation between optical components. Figure 1 shows the Cassegrain layout with a representation of a four segment primary. The optical rays are shown light reflecting from the four primary mirror segments and converge to a secondary mirror, where they are reflected to a focus behind the segmented primary mirrors, located within the cubesat structure. The telescope has a field of view of 0.34 degrees and approximately 3m ground resolution with a swath of 2km, assuming a CCD pixel size of 13μm. Full details of the telescopes optical design characteristics are listed in Table 1.

II.i CCD Selection

After the comparison of CCDs from e2v, Dalsa and Awaiba, a linear TDI (Time delay and Integration) charge Coupled Device image sensor is chosen. It is a device with 2048 pixels. The TDI method increases the sensor responsivity and allow a greater scanning speed in dark conditions [9]. The sensor characteristics are listed in Table 2.

II.ii Optical Performance

Space CCD cameras have been widely used in various types of satellites. The camera includes the lens, the primary mirror, the secondary mirror and other pieces of optical glass. The mechanical structure part is composed of the drawtube, the primary mirror bracket, the secondary mirror bracket, the box and the circuit board. The telescope' electronics tray contains the CCD header board (CCD and thermal control electronics). The associated computing and CCD driver electronics are working separately on the instrument on-board computer (IOBC) to reduce payload size and limit heat dissipation within the telescope itself. CCD detectors are susceptible to noise effects, and dark current effects. Located towards the center of the 3U Nanosatellite, the thermal fluctuations of the CCD are significantly lower than those of components located closer to the surfaces. A passive cooling schemes may be possible even for such a small size and limited power nanosatellite. After the CCD header board was integrated with the rest of the payload and positioned, the adjustment should be done first for the focal position until PSFs of a suitable size are achieved at the target. This adjustment should be done by incrementally adjusting all focusing nuts. During the active segment of the lift off of launch vehicle, the nanosatellite will be affected by the random vibration excitation by the rocket engine thrust, the turbulent boundary layer noise and jet noise. The high frequency jitter in the local optical components will have an influence on the performance of the well adjusted in the ground. An finite element analysis and the simulation of the random disturbance should be offered to guarantee the imaging quality of the system. The current optical design is shown in Fig 1.

III   STRUCTURE DESIGN

Nanosatellite structural design should consider the launcher's constraints, mission requirements and subsystem function requirements. According to mission design, the basic structural design of the satellite should be considered with structural analysis and thermal analysis. The structural analysis should consider the modeling for finite element methods, dynamic analysis, static analysis and thermal strain analysis. The mechanical environment test such as static load test, sinusoidal vibration and acoustic testing should be done. In this research, we only consider the dynamic analysis with possible vibration suppression.

III.i Mechanical Deployable Structure

In the late 1990s, NASA Langley Research Center (LaRC) and the University of Colorado (CU) initiated a deployable optical system [10]. The James Webb Space Telescope and some recent next generation space telescope designs have provided us with some solutions to expand the space telescope [11] [12]. A smaller diameter telescope is ideally suited for multi-satellite launches to save launch costs. The mechanical design of the UK ATC instrument is to ensure that maximum integration flexibility as shown in Fig 2. The mirrors were built with diamond turning material. Diamond turning is a process of mechanical machining of precision elements using Computer Numerical Control (CNC) lathes equipped with natural or synthetic diamond-tipped
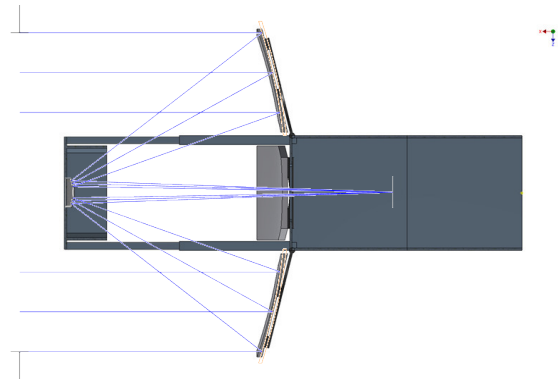

Figure 1. Optical Cassegrain Optics Design

cutting elements. With a low coefficient of thermal expansion and high specific stiffness and strength, diamond turning mirrors were selected as the material for the mirrors. One of the other possible mirror solutions is Actuated hybrid mirrors [13]. Actuated hybrid mirrors are hybrid structures using a precision nanolaminate file facesheet with a silicon carbide substrate equipped with embedded electroactive ceramic actuators. This structure provides the possibility of shape control. The researchers at UK ATC and Heriot Watt University have been working on a prototype of a scalable and potentially low cost stacked array piezoelectric deformable mirror [14]. Folding mirror concepts are simple, buy the implementation is really challenging for nanosatellites. The design of the telescope with folding mirrors is based on the principle that the power or photon flux collected by the telescope is proportional to the area of the aperture [15].

Figs 2, 3, 4 5, 6 and 7 show the nanosatellite with the deployable mirrors with xyz, x/y side view and x/z side view. The deployment includes the boom of the primary mirrors and secondary mirrors. After the first deployment, the satellite will use a ADCS system to achieve three axis stabilization. When the mirror support structure is deployed, the deployment error is always existent. The correction of the misalignment to get images with high quality are necessary. One of the possible solutions is to use piezoelectric actuators for the micro adjustment of the mirrors. In this paper, the micro adjustment of the mirrors are not considered.

IV   SPACECRAFT-LEVEL OPERATIONS SEQUENCE

The satellite command and data handling interconnect is show in Fig 8. The attitude determination and control system operates in several different control modes. This satellite will be inserted in a 350 km and high inclination orbit. It starts in "'Damp Rates'" mode. The angular rate of the satellite is slowed down with the magnetic rods until the reaction wheel can capture the satellite. The satellite then uses "'Sun Acquisition'" mode. The solar
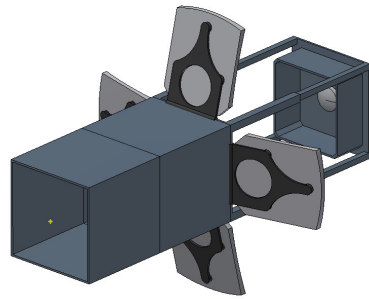
Figure 2. 3U Nanosatellite with the deployable primary mirrors xyz view (secondary mirrors)
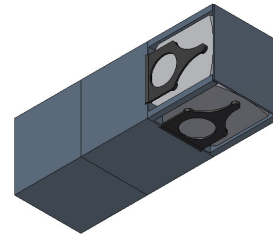

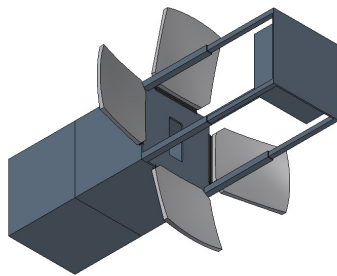Figure 4. 3U Nanosatellite folded Telescope xyz view

Figure 3. 3U Nanosatellite Telescope with the deployable primary mirrors xyz view
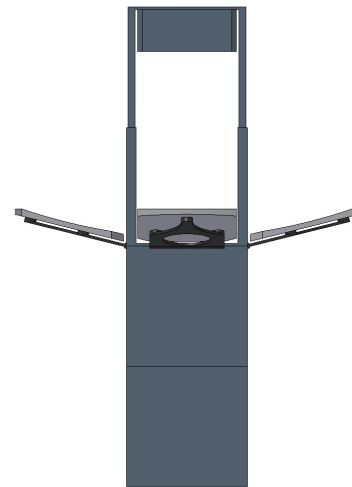

Figure 5. 3U Nanosatellite with the deployable mirrors xz view

panel will recharge the batteries. The Extended Kalman filter will initialize and estimate the turn attitude. The CCD and mirrors' states should be estimated in this mode as well. Once the necessary calibrations are complete. The deployable mirrors will be deployed slowly. The calibration and attitude control operation will be used to achieve stability. During the orbit day, the satellite points the solar panel toward the sun, charges its batteries, and desaturates the reaction wheels to their normal rates in the "'Sun pointing"' mode. As the satellite pass the certain location on the Earth, the satellite will slew and point the nadir. The targets will be observed with the CCD detector. Additional time is allowed after the slew to damp any residual angular rates of the satellite during the "'Target Acquisition Slew"' mode. The next mode is "'Science
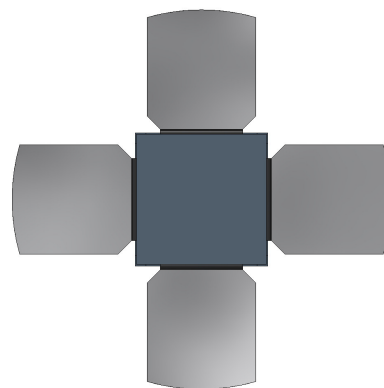

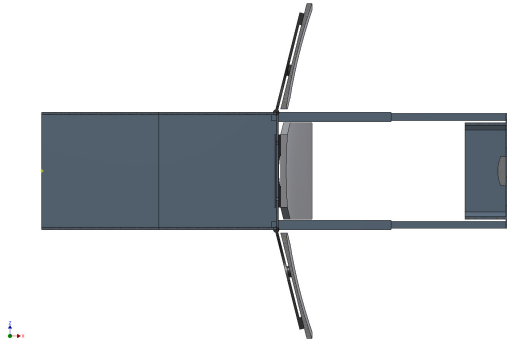Figure 6. 3U Nanosatellite Telescope xy view
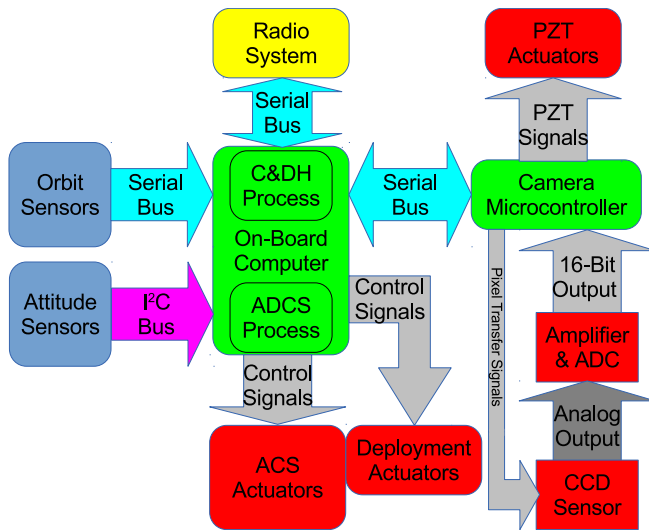
Figure 7. 3U Nanosatellite Telescope yz view

Figure 8. Command and Data Handling Interconnect Diagram

data Collection'" mode. The precise pointing during this mode is achieved by controlling the reaction wheel and piezoelectric mirrors and piezoelectric stage beside the CCD detector. Finally, the data is collected using the CCD camera and downloaded to the ground station.

V ATTITUDE AND POINTING CONTROL SYSTEM

A large telescope satellite attitude control system has been designed in the form of feedback and feed forward interconnected multidimensional control loops [17] [18] [19]. The satellite processes the precision attitude and rate sensor data to generate torque commands for the reaction wheels or control moment gyroscopes. The pointing control system has four major elements, the command generator, the control system, the attitude reference processing, the momentum management. It also includes an image stabilization system using a precision optical mechanical system with fine piezoceramics or piezoelectric micro drives. The image stabilization system consists

of a correlation tracker and a piezo driven tip tilt mirror with servo control electronics. Piezoceramics are ceramic actuators that directly convert electrical energy into small linear motions [20]. The tip tilt mirror mechanism and the focal plane package are located in the beam behind the primary mirrors. For a small telescope, the attitude and pointing control should be miniaturized due to the limited power and volume [21]. There are four control systems for this system: an attitude control system (ACS), fast steering mirror control, dynamic piezoelectric control (DPC) and petal control for the segmented mirrors. ACS and DPC are considered in this paper. The fast steering mirror control and petal control for the segmented mirrors will be considered in future work.

V.i Mathematical Model of Nanosatellite

The spacecraft is modeled as a rigid body with reaction wheels that provide torques about three mutually perpendicular axes that define a body-fixed frame B (shown in Fig. 9).

The equations of motion (shown in Fig. 9) are given by

$$\hat{J}\dot{\omega} = -\omega^\times(J_s\omega + A_i J_w \Omega) + A_i\tau_w + \tau_m + d \quad (1)$$

$$\dot{q} = \frac{1}{2}\begin{pmatrix} q_4 I_{3\times3} + \bar{q}^\times \\ -\bar{q}^T \end{pmatrix}\omega \equiv \frac{1}{2}A(q)\omega \quad (2)$$

$$\begin{bmatrix} \dot{\psi} \\ \dot{\alpha} \\ \dot{\gamma} \end{bmatrix} = \begin{bmatrix} 1 & sin(\psi)tan(\alpha) & cos(\psi)tan(\alpha) \\ 0 & cos(\psi) & -sin(\psi) \\ 0 & sin(\psi/cos(\alpha)) & cos(\psi)/cos(\alpha) \end{bmatrix}\omega \quad (3)$$

where $\omega = (\omega_1, \omega_2, \omega_3)^T$ is the angular velocity of the spacecraft with respect to an inertial frame I and expressed in the body frame B, Ω is the angular velocity of a reaction wheel, $J_s \in R^{3\times3}$ is the inertia matrix of the spacecraft, $\hat{J} = J_s - A_i J_w A_i^T$; $\tau_w \in R^3$ is the control torque distributed between wheel torques; $\tau_m \in R^3$ is the magnetic torques, A_i is the 3×4 or 3×3 (depending on the layout and the number of reaction wheels) matrix whose columns represent the influence of each reaction wheel on the angular acceleration of the satellite, $d \in R^3$ is the bounded external disturbance (including solar radiation pressure disturbance, aerodynamic drag, and gravity gradient torque), $x^\times \in R^{3\times3}$ represents the cross product operator for a vector $x = (x_1, x_2, x_3)^T$ given as

$$x^\times = \begin{pmatrix} 0 & -x_3 & x_2 \\ x_3 & 0 & -x_1 \\ -x_2 & x_1 & 0 \end{pmatrix} \quad (4)$$

and the unit quaternion $q = (\bar{q}^T, q_4)^T = (q_1, q_2, q_3, q_4)^T$ represents the attitude orientation of a rigid spacecraft in the body frame B with respect to the inertial frame I, which is defined by

$$\bar{q} = (q_1, q_2, q_3)^T = e\sin(\theta/2), \quad q_4 = \cos(\theta/2) \quad (5)$$

where e is the Euler axis, and θ is the Euler angle. ψ is the roll angle about the x-axis. α is the pitch angle about the y-axis. γ is the yaw about the z-axis. The unit quaternion
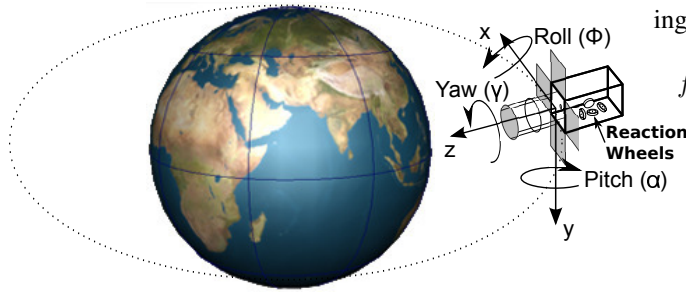
Figure 9. Orbital Coordinate Systems for 3U CubeSat

q satisfies the constraint

$$q^T q = 1 \qquad (6)$$

The torques generated by the reaction wheels τ are given by

$$\tau_w = J_w(\dot{\Omega} + A_i^T \dot{\omega}) \qquad (7)$$

Remark: Based on the deployable structure of the nanosatellite with mirrors and the operation principle, a finite element method will be used to analyze the system schemes.

To address the attitude tracking problem, the attitude tracking error $q_e = (\bar{q}_e^T, q_{4e})^T$ is defined as the relative orientation between the body frame *B* and the desired frame *D* with orientation $q_d = (\bar{q}_d^T, q_{4d})^T$, and it is computed by the quaternion multiplication rule as

$$\bar{q}_e = q_{4d}\bar{q} - q_4\bar{q}_d + \bar{q}^\times \bar{q}_d \qquad (8)$$
$$q_{4e} = q_{4d}q_4 + \bar{q}_d^T \bar{q} \qquad (9)$$

where $q_d \in R^4$ and $q_e \in R^4$ satisfy the constraints $q_d^T q_d = 1$ and $q_e^T q_e = 1$, respectively. The corresponding rotation matrix is given by

$$C(q_e) = \left(q_{4e}^2 - \bar{q}_e^T \bar{q}_e\right) I_{3\times3} + 2\bar{q}_e \bar{q}_e^T - 2q_{4e}\bar{q}_e^\times \qquad (10)$$

Note that $\|C\| = 1$ and $\dot{C} = -\omega_e^\times C$, where $\omega_e = \omega - C\omega_d$ is the relative angular velocity of *B* with respect to *D*, and $\omega_d \in R^3$ is the desired angular velocity.

In order to apply the proposed control algorithm, the equations of motion have to be rewritten as

$$\ddot{\bar{q}}_e = 2(T^{-1})^T[\hat{J}^{-1}(-\omega \times (J_s\omega + A_i J_w \Omega)$$
$$+ A_i\tau_w + \tau_m + d] - 4(T^{-1})^T(\dot{T}^{-1})\dot{\bar{q}}_e \qquad (11)$$

where $T = [q_{4e}I + (\bar{q}_e)^\times]^{-1}$ and $T \neq 0$.

The dynamics equation for nonlinear controller design can be written as:

$$\ddot{\bar{q}}_e = f_i(\bar{q}_e, \dot{\bar{q}}_e) + (\bar{\tau}_w + \bar{\tau}_m) + \bar{d} \qquad (12)$$

A dynamic model of the satellite's relative attitude track-

ing is represented by a diagonal matrix E.

$$f(\bar{q}_e, \dot{\bar{q}}_e) = 2(T^{-1})^T[J^{-1}(-\omega \times (J_s\omega + A_i J_w \Omega)]$$
$$- 4(T^{-1})^T(\dot{T}^{-1})\dot{\bar{q}}_e + 2(T^{-1})^T J^{-1}\omega \times \omega \qquad (13)$$

$$\bar{\tau}_w = E[2(T^{-1})^T J^{-1} A_i \tau_w] \qquad (14)$$

$$\bar{d} = 2(T^{-1})^T J^{-1} d \qquad (15)$$

$$\bar{\tau}_m = 2(T^{-1})^T J^{-1} \tau_m \qquad (16)$$

V.ii   Measurement Sensor Model of the Nanosatellite

V.ii.i   The Magnetometer Model

The magnetic field vectors are obtained in the orbit reference frame [22]:

$$B_1 = \frac{M_e}{r_0^3}[cos(\omega_0 t)(cos(\varepsilon)sin(i) - sin(\varepsilon)cos(i)cos(\omega_e t))$$
$$- sin(\omega_0 t)sin(\varepsilon)sin(\omega_e t)] \qquad (17)$$

$$B_2 = -\frac{M_e}{r_0^3}[(cos(\varepsilon)cos(i) + sin(\varepsilon)sin(i)cos(\omega_e t))$$
$$\qquad (18)$$

$$B_3 = \frac{2M_e}{r_0^3}[sin(\omega_0 t)(cos(\varepsilon)sin(i) - sin(\varepsilon)cos(i)cos(\omega_e t))$$
$$- 2sin(\omega_0 t)sin(\varepsilon)sin(\omega_e t)] \qquad (19)$$

where ω_0 is the angular velocity of the orbit with respect to the inertial frame. r_0 is the distance from the center of the satellite to the center of the Earth. i is the orbit inclination. ε is the magnetic dipole tilt. ω_e is the spin rate of the Earth. M_e is the magnetic dipole moment of Earth. The magnetometer model should be:

$$H(\psi, \alpha, \gamma, t) = C_k \begin{bmatrix} B_1 \\ B_2 \\ B_3 \end{bmatrix} + \eta_m \qquad (20)$$

where C_k is the direction cosine matrix in terms of Euler Angles [22]. η_m is the zero mean Gaussian white noise of the magnetometer.

V.ii.ii   The Rate Gyro Model

The angular velocity is measured from three rate gyros. A well-known model for the angular velocity measurement is given by

$$\omega_g = \omega + b_g + \eta_g \qquad (21)$$

where $\eta_g \in R^3$ is the output of the gyro, and ω is the real angular rate of the gyro, η_g and η_f are independent Gaussian white noise with zero mean and standard deviation. b_g is the random drift. k_f is a constant number.

$$\dot{b}_g = -k_f \times b_g + \eta_f \qquad (22)$$

V.iii   Satellite Atmospheric Drag

The main disturbances are thermal distortion, gravity drag, sensor and actuator noise, reaction wheel vibration, atmospheric (aerodynamic drag) turbulence and wind.

The aerodynamic drag has an influence on the motion of the low Earth orbit satellites (lower than 400 km). The aerodynamic force in continuum flow can be expressed in terms of the drag, i.e. the force parallel to the atmospheric velocity direction. The vector equation for computing the drag force

$$\vec{F}_{drag} = -\frac{1}{2}\rho C_d \frac{A}{m} V_{rel}^2 \frac{\vec{V}_{rel}}{\left|\vec{V}_{rel}\right|} \qquad (23)$$

where C_d is the drag coefficient, ρ is the atmospheric density, and A is the projected area of the satellite normal to $\vec{V}_{rel}$. $\vec{V}_{rel}$ is the relative velocity of the satellite with respect to the atmosphere. Here it is assumed that the atmosphere is stationary with respect to the Earth and also that the $\vec{V}_{rel}$ has a component only along the y-axis. The drag force $\vec{F}_{drag}$ thus acts in the direction opposite to the relative velocity $\vec{V}_{rel}$. The coefficient C_d is dependent on the geometry of the satellite and varies with altitude, Mach number and the angle of attack. These parameters are chosen in this paper according to the data in References [23] [24] and [25].

The aerodynamic torque on the satellite can be calculated using

$$\vec{\tau}_{drag} = \Sigma \vec{r}_j \times \vec{F}_{drag} \qquad (24)$$

where r_j is the position error of the geometric center of the individual drag panels (mirrors) measured from the satellite center of mass.

The density is

$$\rho = \rho_o exp(-\frac{y - y_0}{H}) \qquad (25)$$

y is an altitude above the reference surface (Earth). y_0 is the altitude at geocentric distance. H is the scale height:

$$\frac{1}{H} = \frac{1}{h} - \frac{2}{r_0} \qquad (26)$$

$$h = \frac{R_0 T}{Mg} \qquad (27)$$

where T is the local atmospheric temperature. M is the molecular mass. R_0 is the universal gas constant. H has a firm relation with temperature.

V.iv   Reaction Wheel Disturbance

Generally, reaction wheels are considered to be the largest micro vibration sources for a spacecraft. The Hubble Space Telescope used a Honeywell passive isolator for suppressing the vibrations from reaction wheels. Many different types of vibration isolator have been used for space telescopes.

It is important to calculate the magnitude of the reaction wheel vibrations to determine how much these vibrations will affect the pointing of the satellite. The disturbances are modeled as:

$$d_i(t) = \sum_i^n c_i \omega_{RW}^2 sin(2\pi h_i \omega_{RW}(t) + \varphi_i) \qquad (28)$$

where c_i is the coefficient of the ith harmonic, h_i is the harmonic number of the ith harmonic, ω_{RW} is the speed of the reaction wheel, and φ is the uniformly distributed random variable over the domain. Each reaction wheel produces radial disturbances. The harmonics and their corresponding coefficients are wheel dependent and are determined experimentally. In References [26] and [27], the experiment analysis and simulation analysis of the reaction wheel vibration performance gives some examples of the influences of such actuators for jitter analysis.

V.v   Piezoelectric Stage Design for Micro-vibration

The mirrors will experience the disturbance vibrations on orbit from reaction wheels and other moving mechanisms. These vibration could be in the form of accelerations of the mirrors' boundary conditions that induce shape deformations visa internal inertial forces. Ideally, the mirror wheels should be despun to the lowest practical speeds in order to minimize resonances with the flexible mirrors. The additional sensor and actuators swill be used for the shape control with the satellite attitude control systems.

V.v.i   Piezoelectric Sensor Model

When piezoelectric materials are used as a sensor, a mechanical strain plays a role as both input to and output from the electrical voltage. The voltage is corrected to the desired shape which is used as the controller input. The controller output affects the actuator which will prevent the vibrations [29].

Linear piezoelectric coupling between the elastic field and electric field can be expressed as following [30]

$$D_z = e_{31}\sigma + e_\sigma E_f \qquad (29)$$

$$\varepsilon = d_{31}E_f + S_E\sigma \qquad (30)$$

where D_z is the electric displacement, d_{31} is the piezoelectric constant, σ is the stress, e is permittivity, E_f is the electric field, ε is the strain, and s_E is the piezoelectric medium softness.

Sensor current is given as

$$i(t) = \frac{d}{dt} \int e_{31} \varepsilon_x dA \qquad (31)$$

$$\varepsilon = d_{31} E_f + S_E \sigma \qquad (32)$$

where i is generated by the total charge $Q(t)$. ε_x is a specific point in terms of second location derivative of displacement function $w''(x,t)$. Consider $\varepsilon_x = z\frac{d^2 w}{d^2 x}$, Equation 32 can be written as:

$$i(t) = z e_{31} b \int_0^{l_p} [n_1]^T \dot{q} dx \qquad (33)$$

The sensor voltage $V^s(t)$ can be written as

$$V^s(t) = G_c z e_{31} b \int_0^{l_p} [n_1]^T \dot{q} dx \qquad (34)$$

where G_c is the modified signal parameter. Let $S_1 = G_c z e_{31}$, $V^s(t)$ can also be written as $S_1 \int_0^{l_p} [n_1]^T \dot{q} dx$.

V.v.ii PZT Actuator Model

PZT sensor output voltage will be given to the controller. The controller output signal is equal to the controller gain (k) multiplied by the sensor voltage. The PZT actuator output signal $V^a(t)$ can be written as $S_2 \int_0^{l_p} [n_1]^T \dot{q} dx$, where $S_2 = KV^s(t)$. t_p is the Piezo layer thickness, t_s is the sensor thickness. t_a is the actuator thickness. When the input voltage $V^a(t)$ in the t_a thickness direction, the electric field E_f and tension σ_a are written as

$$\sigma_a = E_p d_{31} E_f = E_p d_{31} \frac{V^a(t)}{t_a} \qquad (35)$$

Where E_p is the Young's modulus of the piezoelectric layer.

The bending stress σ_a is the source of the bending moment M_a in the piezoelectric actuator element.

$$M_a = E_p d_{31} \bar{z} b V^a(t) \qquad (36)$$

Let $S_3 = E_p d_{31} \bar{z} b$, M_a can be written as $S_3 V^a(t)$.

The torque which is applied to the dynamic system can be written as

$$\tau_a = E_p d_{31} \bar{z} b \int [n]' dx V^a(t) \qquad (37)$$

V.v.iii Modeling for Vibration Suppression

The satellite PZT stage is assumed as flexible beams with a head stuck (one end fixed). The beam is covered with a layer of PZT sensors and actuators. The strain energy and Kinetic energy of the bended beam element with uniform crossover is obtained from the following equations

$$\frac{d}{dt}\left[\frac{\partial T}{\partial \dot{q}_i}\right] + \frac{\partial U}{\partial q_i} = Z_i \qquad (38)$$

where

$$U = E_b I_b \int \left[\frac{\partial^2 w}{\partial^2 x}\right]^2 dx \qquad (39)$$

$$T = \frac{\rho_b A_b}{2} \int \left[\frac{\partial w}{\partial t}\right]^2 dx \qquad (40)$$

where $w(x,t)$ is the deflection of the beam at point x. t denotes time.

$$w(x,t) = \sum_0^{m \to \infty} \phi_k(x) q_k(t) \qquad (41)$$

where $\phi(x)$ is the normal function. $q_k(t)$ is the generalized flexible coordinate. k is the representing of the mode number $(k = 1..m)$.

The simple basic beam model is

$$\bar{M}_b \ddot{q}_b + \bar{K}_b = \tau_b \qquad (42)$$

where $\ddot{q}_b$ is the acceleration vector. $\bar{M}_b$ is the mass vector matrices. $\bar{K}_b$ is the stiffness vector matrices.

$$\bar{M}_b = \rho_b A_b \int [n]^T [n] dx \qquad (43)$$

$$\bar{K}_b = E_b I_b \int [n_1]^T [n_1] dx \qquad (44)$$

For piezoelectric beam elements, the model is

$$\bar{M}_p \ddot{q}_p + \bar{K}_p = \tau_p \qquad (45)$$

For smart beam elements, the model is

$$\bar{M}_s \ddot{q}_s + \bar{K}_s = \tau_s \qquad (46)$$

where $\bar{M}_s = \rho_s A_s \int [n]^T [n] dx$, $\bar{K}_s = E_s I_s \int [n_1]^T [n_1] dx$, $\rho_s A_s = b(\rho_b A_b + 2\rho_p A_p)$. and $E_s I_s = E_b I_b + 2E_p I_p$.

V.v.iv   PZT Control

Usually, using a minimum number of PZT actuators (one PZT actuator), the beam is assumed to keep angle zero relative to the horizon. All rises and dips are zero. The beam is under the control of a torque at angle θ_D. The PID torque is

$$\tau_D = \bar{k}_p(\theta_2 - \theta_1) + \bar{k}_d(\dot{\theta}_2 - \dot{\theta}_1) + \bar{k}_I \int (\theta_2 - \theta_1)dt \quad (47)$$

where $\bar{k}_p$, $\bar{k}_d$ and $\bar{k}_I$ are PID gains. Define $\theta_2 = \theta_D$. $\dot{\theta}_2 = 0$. $\theta_1 = \dot{\theta}_1 = 0$.

Using multi-hub and structure control input, the principle is the same as using one PZT actuator. A specific torque is applied to the hub using Equation 47. The PID controller using PZT sensor voltage can be written as

$$V^a(T) = \bar{k}_p V^s(t) + \bar{k}_d \dot{V}^s(T) + \bar{k}_I \int V^s(t)dt \quad (48)$$

V.vi   Satellite Attitude Control System

For a nanosatellite telescope structure design, the whole satellite vibration isolation and shock isolation should be considered. The shock isolation have been designed for frequencies above 100 HZ. The whole satellite vibration isolation is designed to attenuate frequencies above 30 HZ. Light weight space telescopes have become popular. Lighter optics can increase susceptibility to low frequency vibration disturbances. The support structure must be stiff for the lighter optics. As a result, small nonlinearities of the structure become large problems [31]. Vibration reduction for flexible spacecraft by input shaping [32], adaptive control [33] and positive position feedback (PPF) control is proposed for attitude maneuvers. Using Lyapunov stability and dissipativity theory, control systems for slewing and vibration suppression have been developed. Vibration reduction using reaction wheels and thrusters have been proposed for the space telescope NGST. The thrusters were used for momentum dumping of the reaction wheels. The nanosatellite vibration isolation should design for the frequencies 0.1 Hz to 1 HZ. Our satellite attitude control system is based on Lyapunov stability theory. Four reaction wheels are used for the precise pointing of the space camera. In our work, three magnetic rods are used for detumbling mode. The magnetic rods are also used for the momentum dumping of the micro reaction wheels. The deployable mirrors are handled after the detumbling mode. Second, a coarse attitude control is actuated with reaction wheels for pointing the satellite to a target object. Finally, a precision position control of the image sensor using the piezoelectric stage actuator behind the CCD detector will be used for high resolution observation.

The adaptive nonlinear controller is used to achieve or maintain an acceptable level for the performance of control systems when the satellite dynamics have unknown parameters due to the disturbances. The sliding mode can be defined by the following nonlinear differential equation:

$$S = \lambda_1 \dot{\bar{q}}_e^{\frac{p}{q}} + \bar{q}_e + \lambda_2 sign(\bar{q}_e) \quad (49)$$

where λ_1 and λ_2 are the parameters to be designed.

The adaptive parameter θ can be updated by the following adaptive laws:

$$\dot{\theta} = \alpha \lambda_2 \rho \dot{q}_e^{\rho-1} s\xi \quad (50)$$

$$\xi = \frac{\prod_{i=1}^{N} \mu_{A_i^l(s)}}{\sum_{l=1}^{P} \prod_{i=1}^{N} \mu_{A_i^l(s)}} \quad (51)$$

where α is a positive constant and $\rho = p/q$.

In order to guarantee that the estimated Fuzzy Logic System parameters remain within some known bounded sets, a smooth projection is considered in this paper. Let θ be the estimation of the optimal weight matrix θ^*, and define a smooth projection of θ as:

$$\pi(\theta) = \theta_\pi = \pi_{jk}(\theta_{jk}), j = 1, 2, ..., m, k = 1, 2, ..., N_1 \quad (52)$$

Each projection operator π_{jk} is a real-value smooth non-decreasing function defined by

$$\pi_{jk}(\theta_{jk}) = \theta_{jk},$$
$$\forall \theta_{jk} \in [\theta_{min}, \theta_{max}]$$
$$\pi_{jk}(\theta_{jk}) \in [\theta_{min} - \varepsilon_{Mi}, \theta_{max} + \varepsilon_{Mi}] \quad (53)$$

Define $\tilde{\theta} = \theta^* - \theta$, $\tilde{\theta}_\pi = \theta^* - \theta_\pi$, and

$$V_\theta = \frac{1}{\delta} \sum_{j=1}^{m} \sum_{k=1}^{N_1} \int_0^{\tilde{\theta}} (\theta^*_{jk} - \pi_{jk}(\theta^*_{jk} - \omega_{jk})d\omega_{jk},$$
$$i = 1, 2, ..., n \quad (54)$$

where, V_θ is positive definite with respect to $\tilde{\theta}_{jk}$ for $\theta^*_{jk} \in [\theta_{min}, \theta_{max}]$. Furthermore,

$$\dot{V}_\theta = -\frac{1}{\delta} \sum_{j=1}^{m} \sum_{k=1}^{N_1} \tilde{\theta}_{\pi,jk} \dot{\theta}^*_{jk}, i = 1, 2, ..., n \quad (55)$$

The adaptive nonlinear controller of the satellite is now given by [34]

$$\tau_{AMC} = -k_1 s - k_2 s^\rho - \frac{q}{p} s^{2-\frac{p}{q}} \theta^T \xi - \psi \quad (56)$$

where s is the sliding surface. ξ is built using fuzzy membership functions. $H_r = \theta^T \xi$ is the estimation of the uncertain nonlinear dynamics function by a fuzzy logic system. $\psi = \kappa tanh(\frac{3K_u \kappa s}{\epsilon})$. α, κ, ϵ are positive constant

numbers.

V.vi.i   Stability Analysis

Theorem: In the system Eq. (12), the nonlinear control laws defined by Eqs. 56, with adaptive control laws given by Eq. (50) guarantee that all signals of the closed loop system are bounded.

Proof of Theorem: The dynamics equations for the quaternion errors of the satellite can be written as:

$$\bar{q}_e = e_1 \quad \dot{\bar{q}}_e = e_2 \tag{57}$$

$$\dot{e}_1 = e_2 \quad \dot{e}_2 = f(\bar{q}_e, \dot{\bar{q}}_e) + \hat{\tau} + \Delta\tau + \nu \tag{58}$$

Using Eq. (49), we obtain

$$\dot{s} = \dot{e}_1 + \lambda_2\rho\dot{e}_1^{\rho-1}(f + \hat{\tau} + \Delta\tau + \nu) \tag{59}$$

Using the approximation property of fuzzy logic systems and substituting the control law Eqs. (56) into the error dynamics Eq. (12) yields the following dynamic equation for sliding surface s.

$$
\begin{aligned}
\dot{s} &= \dot{e}_1 + \lambda_2\rho\dot{e}_1^{\rho-1}(F - F_d + F_d - \theta^T\xi - K_1 s - K_2 s^\rho \\
&\quad - \frac{1}{\rho\lambda_2}\dot{e}_1^{2-\rho} - \varphi + \nu + \Delta\tau) \\
&= \lambda_2\rho\dot{e}_1^{\rho-1}(\varsigma + \tilde{\theta}^T\xi - K_1 s - K_2 s^\rho \\
&\quad - \varphi + \nu + \varepsilon + \Delta\tau)
\end{aligned}
\tag{60}
$$

where $\varsigma = F - F_d$.

The following Lyapunov function candidate

$$V = \frac{1}{2}s^T s + V_\theta \tag{61}$$

has the time derivative

$$\dot{V} = s^T\dot{s} + \dot{V}_\theta \tag{62}$$

Due to the fact that

$$s^T\lambda_2\rho\dot{e}_1^{\rho-1}\tilde{\theta}^T\xi - \frac{1}{\delta}\sum_{j=1}^{m}\sum_{k=1}^{N_1}\tilde{\theta}_{F_{\pi,jk}}\dot{\theta}_{jk}^* = 0 \tag{63}$$

We can substitute Eqs. (55) and (60) into Eq. (62), to obtain:

$$
\begin{aligned}
\dot{V} &= \lambda_2\rho\dot{e}_1^{\rho-1}(s^T\varsigma + s^T\tilde{\theta}^T\xi - s^T K_1 s - s^T K_2 s^\rho - s^T\varphi \\
&\quad + s^T(\nu + \varepsilon + \Delta\tau) - \frac{1}{\delta}\sum_{j=1}^{m}\sum_{k=1}^{N_1}\tilde{\theta}_{F_{\pi,jk}}\dot{\theta}_{jk}^*) \\
&= \lambda_2\rho\dot{e}_1^{\rho-1}(s^T\varsigma - s^T K_1 s - s^T K_2 s^\rho - s^T\varphi \\
&\quad + s^T(\nu + \varepsilon + \Delta\tau))
\end{aligned}
\tag{64}
$$

Using the inequality in reference, it is easy to obtain

$$-s^T\varphi + s^T(\nu + \varepsilon + \Delta\tau) \le n\epsilon \tag{65}$$

The well-known inequality

$$\left(\sqrt{\bar{\psi}}s - \frac{\varsigma}{2\sqrt{\bar{\psi}}}\right)^T\left(\sqrt{\bar{\psi}}s - \frac{\varsigma}{2\sqrt{\bar{\psi}}}\right) \ge 0 \tag{66}$$

can be rewritten as

$$s^T\varsigma \le \bar{\psi}s^T s + \frac{\varsigma^2 M}{4\bar{\psi}} \tag{67}$$

where $\bar{\psi}$ is a positive constant satisfying $\bar{\psi} < \lambda_{min}(K_1)$ with $\lambda_{min}(K_1)$ being the minimum eigenvalue of the matrix K_1. Eq. (64) becomes

$$
\begin{aligned}
\dot{V} &\le \lambda_2\rho\dot{e}_1^{\rho-1}(-(\lambda_{min}(K_1) - \bar{\psi})s^T s + \hat{\psi} - s^T K_2 s^\rho) \\
&\le -\sigma_2\rho\dot{e}_1^{\rho-1}M_{2i}|s|^2 \le 0
\end{aligned}
\tag{68}
$$

where $\hat{\psi} = n\epsilon + \frac{\varsigma^2 M}{4\psi}$ is a positive constant.

The inequality Eq. (68) implies that the sliding surfaces are bounded. The state errors $\bar{q}_e$ and $\dot{\bar{q}}_e$ are bounded. All signals in the closed-loop system are uniformly ultimately bounded. Thus, we have demonstrated the stability of the overall closed-loop system and have given the stability proof.

VI   SIMULATION RESULTS

In this section, the proposed control methods are used for the problem of attitude control of a nanosatellite telescope. The detailed response of the system is simulated using the set of governing equations of motion and in conjunction with the proposed control algorithm. The satellite with deployable mirrors and reaction wheel parameters are shown in Table 3. The folded, partly deployed, and fully deployed satellite's moment of inertia and the aerodynamic disturbances can shown in Tables 4 and 5. The nonlinear control parameters for Reaction Wheels and Magnetic Rods are shown in Tables 6 and 7.

For the fully deployed all mirrors case, the satellite attitude control system simulation results for tracking the ground target are shown in Figure 10 to Figure 26. Figures 10 to 13 are the simulated results using three axis magnetic rods without the aerodynamic drags (with gravity gradient torque). Figures 14 to 17 are the simulated results using three axis magnetic rods with the aerodynamic drags and gravity gradient torque. It is clear that ACS attitude errors are too large using three axis magnetic rods. Three axis Reaction wheels are considered for this mission. However, the simulation results shows the attitude stability will not be lost without one extra Z axis magnetic rods. Figures 18 to 26 show the Euler Angle tracking errors, control inputs, quaternion tracking errors, reaction wheels speed, wheel voltage, satellite angular velocity, sliding surface, Z axis magnetic rod dipole, and

Z axis magnetic rod torque with the aerodynamic drags and gravity gradient torque. For each orbit, there are 0.1 orbit which the attitude tracking errors are less than 0.0001 deg (0.32 arcsec). The angular velocity tracking errors for each orbit are less than $0.00001\ rad/s$.

Table 3. Fully Deployed Satellite Model Parameters.

Parameters	Values
Orbit	
R_c (km)	6728
μ_e (km^{3}s^{-2})	398600
Size (m^3)	$0.10 \times 0.10 \times 0.34$
Moment of Inertia	
I_{xx} (kg m^2)	0.085170
I_{yy} (kg m^2)	0.085225
I_{zz} (kg m^2)	0.08988
Reaction Wheel	
Mom. of inertia, J$_{\mathrm{wi}}$, (kg m^2)	1×10^{-5}
Max. Voltage, e$_{\mathrm{a,max}}$, (V)	4.5

Table 4. Satellite Deployable Model Parameters.

Parameters	Values
Folded	
I_{xx} (kg mm^2)	$77.669e + 3$
I_{yy} (kg mm^2)	$77.865e + 3$
I_{zz} (kg mm^2)	$6.754e + 3$
Deployed with Primary Mirrors	
I_{xx} (kg mm^2)	$72.149e + 3$
I_{yy} (kg mm^2)	$72.203 + 3$
I_{zz} (kg mm^2)	$8.988e + 3$
Deployed with All Mirrors	
I_{xx} (kg mm^2)	$85.170e + 3$
I_{yy} (kg mm^2)	$85.225e + 3$
I_{zz} (kg mm^2)	$8.988e + 3$

Table 5. Satellite Aerodynamic Disturbance.

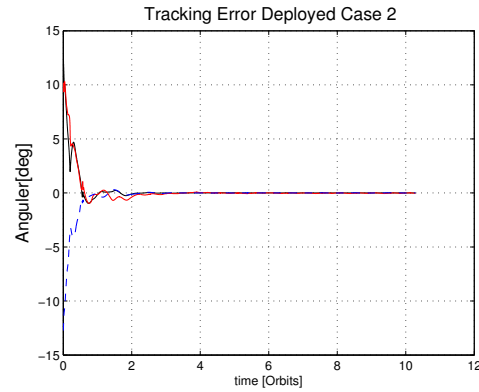| Parameters	Values
Folded	
τ_{xx} (Nm)	0
τ_{yy} (Nm)	0
τ_{zz} (Nm)	$-0.7488e - 6$
Deployed with Primary Mirrors	
τ_{xx} (Nm)	0
τ_{yy} (Nm)	0
τ_{zz} (Nm)	$0.2011e - 6$
Deployed with All Mirrors	
τ_{xx} (Nm)	0
τ_{yy} (Nm)	0
τ_{zz} (Nm)	$0.2695e - 6$

Figure 10. Deployed Primary Mirrors and Secondary Mirror Case: ACS Results using Three Magnetic Rods without Aerodynamic Drag Euler Angler Tracking Errors
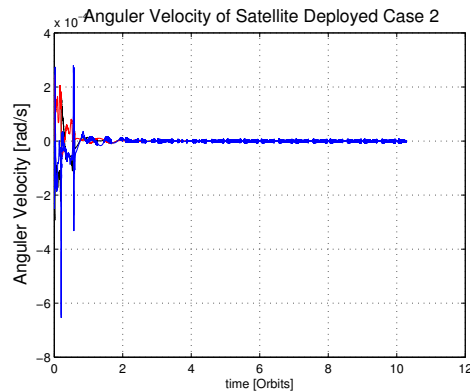

Figure 11. Deployed Primary Mirrors and Secondary Mirror Case: ACS Results using Three Magnetic Rods without Aerodynamic Drag Angular Velocity Tracking Errors
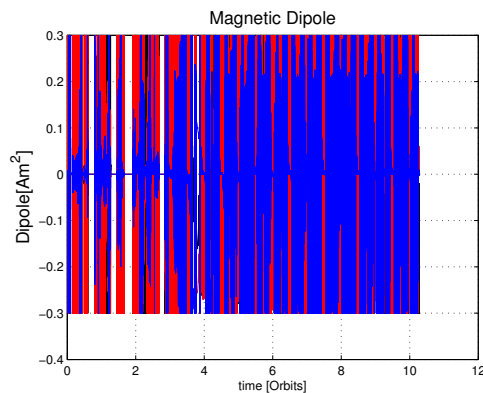

Figure 12. Deployed Primary Mirrors and Secondary Mirror Case: ACS Results using Three Magnetic Rods without Aerodynamic Drag Magnetic Dipoles
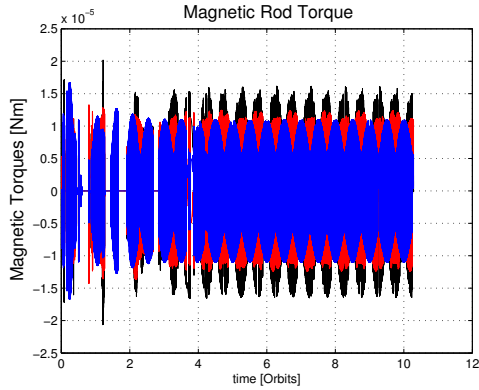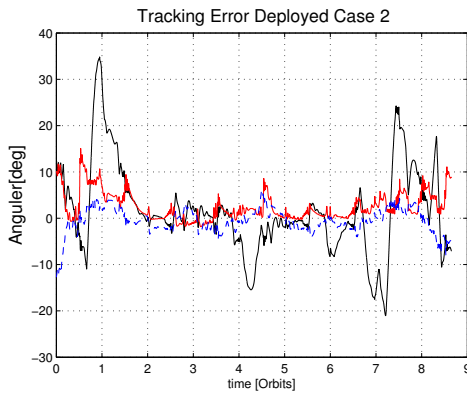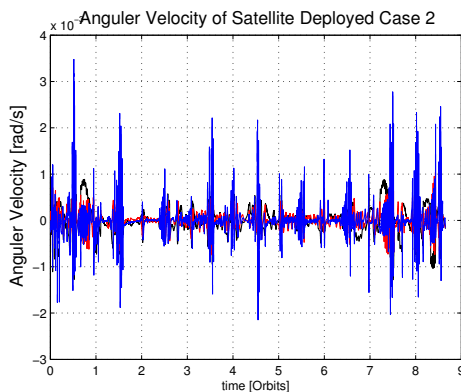
Figure 13. Deployed Primary Mirrors and Secondary Mirror Case: ACS Results using Three Magnetic Rods without Aerodynamic Drag Magnetic Torques

Table 6. Satellite Attitude Controller Parameters for Reaction Wheels.

Parameters	Values
p, q	$11, 9$
κ, ϵ	$0.00001, 0.01$
λ_1, λ_2	10.0000001
k_1	$diag(0.004, 0.004, 0.004)$
k_2	$diag(0.004, 0.004, 0.004)$
$\theta_0, \theta_{min}, \theta_{max}, \alpha$	$0, -200, 200, 2$

Figure 14. Deployed Primary Mirrors and Secondary Mirror Case: ACS Results using Three Magnetic Rods with Aerodynamic Drag Euler Angler Tracking Errors

Figure 15. Deployed Primary Mirrors and Secondary Mirror Case: ACS Results using Three Magnetic Rods with Aerodynamic Drag Angular Velocity Tracking Errors
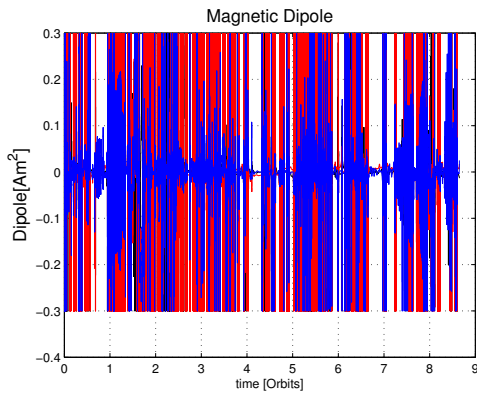
Table 7. Satellite Attitude Controller Parameters for Magnetic Rod.

Parameters	Values
$\bar{\kappa}, \bar{\epsilon}$	$0.1, 1$
$\bar{\lambda}_1, \bar{\lambda}_2$	$0.001, 1$
$\bar{k}_1$	$diag(0.4, 0.4, 0.4)$
$\bar{k}_2$	$diag(0.004, 0.004, 0.004)$
$\bar{\theta}_0, \bar{\theta}_{min}, \bar{\theta}_{max}, \bar{\alpha}$	$0, -10000, 10000, 5e-10$

Figure 16. Deployed Primary Mirrors and Secondary Mirror Case: ACS Results using Three Magnetic Rods with Aerodynamic Drag Magnetic Dipoles
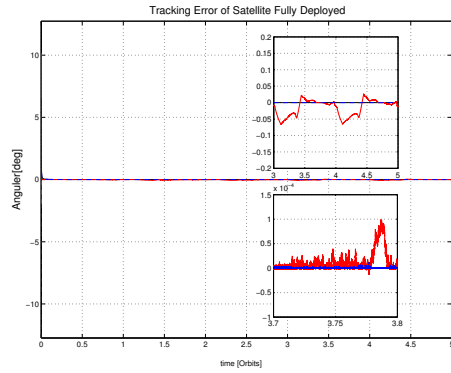

Figure 18. Deployed Primary Mirrors and Secondary Mirror Case with Aerodynamic Torque: ACS Results using Three Reaction Wheels and One Magnetic Rod Euler Angle Tracking Errors
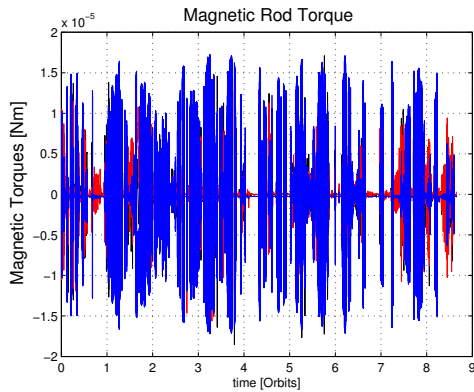

Figure 17. Deployed Primary Mirrors and Secondary Mirror Case: ACS Results using Three Magnetic Rods with Aerodynamic Drag Magnetic Torques
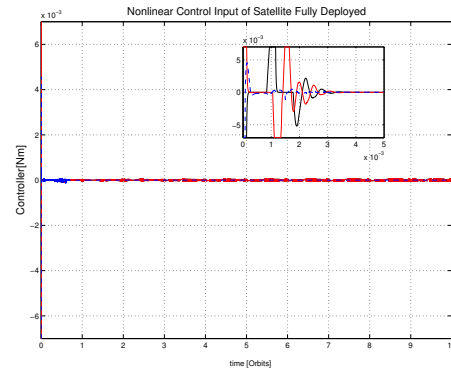

Figure 19. Deployed Primary Mirrors and Secondary Mirror Case with Aerodynamic Torque: ACS Results using Three Reaction Wheels and One Magnetic Rod Control Input

VII CONCLUSIONS

This paper presents a design for attitude tracking of a nanosatellite telescope with deployable mirrors using reaction wheels and PZT sensors and actuators. Although various nonlinear control algorithms have been published in the literature for spacecraft attitude control, very few have addressed the control problems of such small satellites with telescope optics for Earth Observation missions. We considered scenarios of reaction wheel actuator vibration management options and deployable mirrors, varied scenarios that can introduce disturbances into the overall closed-loop system causing the dynamics of the satellite deviate from its nominal regime. To verify and validate the effectiveness of the proposed control method, a high-fidelity nonlinear model of the nanosatellite attitude dynamics was developed which includes the mathematical models of environmental disturbances acting on the satellite in very low Earth orbit. Overall, the results clearly establish the robustness of the proposed control methodologies in tracking the attitude of the spacecraft in the presence of reaction wheel vibrations and aerodynamic uncertainties. A prototype demonstration will be done in
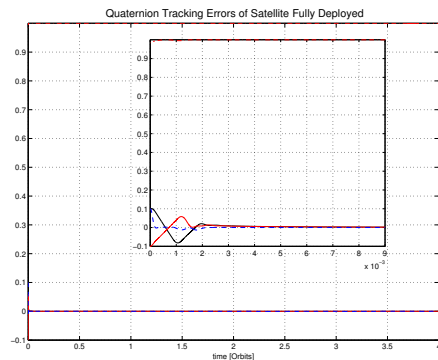

Figure 20. Deployed Primary Mirrors and Secondary Mirror Case with Aerodynamic Torque: ACS Results using Three Reaction Wheels and One Magnetic Rod Quaternion
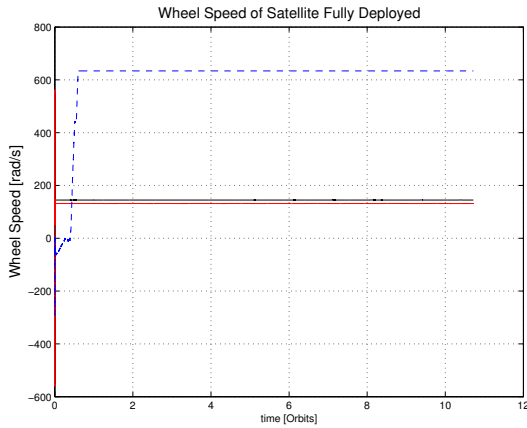
IAC-14-B4, 4.4.25291

Figure 21. Deployed Primary Mirrors and Secondary Mirror Case with Aerodynamic Torque: ACS Results using Three Reaction Wheels and One Magnetic Rod Reaction Wheels Speed
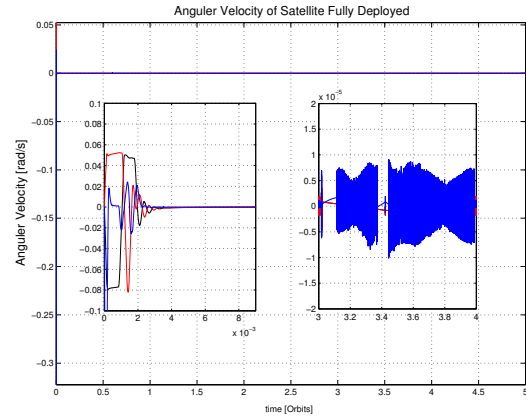

Figure 23. Deployed Primary Mirrors and Secondary Mirror Case with Aerodynamic Torque: ACS Results using Three Reaction Wheels and One Magnetic Rod Angular Velocity
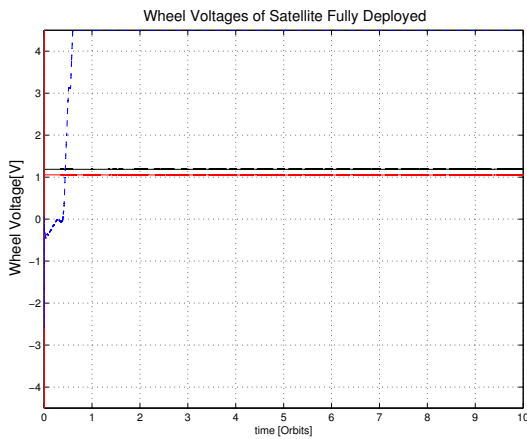

Figure 22. Deployed Primary Mirrors and Secondary Case with Aerodynamic Torque: ACS Results using Three Reaction Wheels and One Magnetic Rod Reaction Wheels Voltage
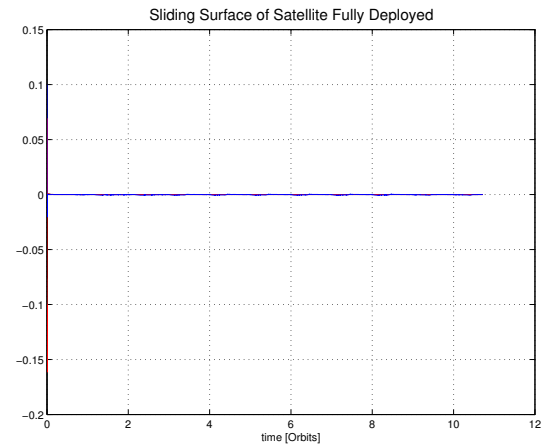

Figure 24. Deployed Primary Mirrors and Secondary Mirror Case with Aerodynamic Torque: ACS Results using Three Reaction Wheels and One Magnetic Rod Reaction Wheels Speed

future work.

VIII   REFERENCES

[1] Selva, D. and Krejci, D., "A Survey and Assessment of the Capabilities of Cubesats for Earth Observation", Acta Astronautica, Vol. 74, 2012, pp 50-68.

[2] Bouwmeester, J. and Guo, J., "Survey of Worldwide Pico and Nanosatellite Missions, Distributions and Subsystem Technology", Acta Astronautica, Vol. 67, No. 7-8, 2010, pp 854-862.

[3] Nakamura, K., Funase, R., Nagai, M., Enokuchi, A., Nojiro, Y., Funane, T., Sasaki, F., and Nakasuka, S., "Extensible Boom Based Optical System for Nano-Scale Remote Sensing Satellite PRISM", 19th Annual AIAA/USU Conference on Small Satellite, SSC05-VI-1, 2005, pp 1-9.

[4] Andersen Geoff, Dearborn Michael and McHarg Geoff, "FalconSAT-7: A Photon Sieve Solar Telescope", USAF Academy.

[5] Agasid Elwood, Rademacher Abraham, McCullar Michael, and Gilstrap, Ray, "Study to Determine the Feasibility of a Earth Observing Telescope Payload for a 6U Nano Satellite", National Aeronautics and Space Administration Report, 2010.

[6] Inamori, T., and Sako, N., and Nakasuka, S., "Attitude Control System for the Nano-astrometry Satellite Nano-JASMINE", Aircraft Engineering and Aerospace Technology, Vol,83, No.4, 2011, pp 211-228.

[7] Baker, A. M., Cawthorne, A., Cutter, M., and Curiel, A.,S., "Reading the Fine Print from Orbit: Its not
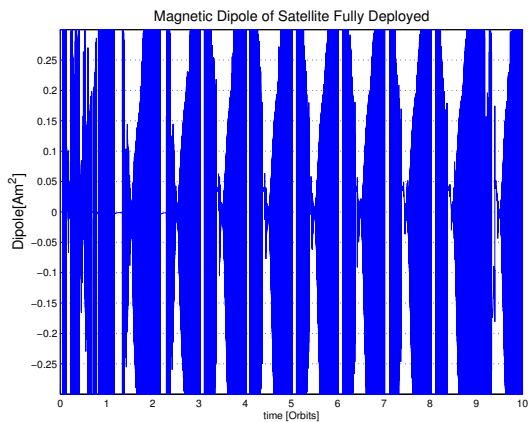
Figure 25. Deployed Primary Mirrors and Secondary Case with Aerodynamic Torque: ACS Results using Three Reaction Wheels and One Magnetic Rod Z-axis Magnetic Dipole
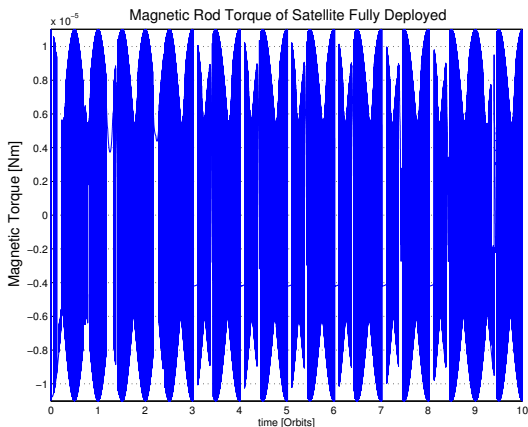

Figure 26. Deployed Primary Mirrors and Secondary Mirror Case with Aerodynamic Torque: ACS Results using Three Reaction Wheels and One Magnetic Rod Z-axis Magnetic Torque

just about the resolutio", 22nd Annual AIAA/USU Conference on Small Satellites, SSC08-IV-5, 2008, PP 1-8.

[8] Santer, M. J., and Seffen, K. A., "Optical Space Telescope Structures: The state of the art and future directions", The Aeronautical Journal, Vol. 113, No. 1148, 2009, pp 1-11.

[9] Zhao, C., Li, C., and Zhou, N., "A Deployalbe Telescope Imaging System with Coilable Tensegrity Structure for Microsatellite Application", International Symposium on Photoelectronic Detection and Imaging 2013, doi:10.1117/12.2033266.

[10] Lake, M. S., Phelps, J. E., Dyer, J. E., Caulde, D. A., Tam A., Escobedo, J., Kasl, E. P., "A deployable Primary Mirror for Space Telescipes", Proceedings of the SPIE-3785-02, Dever, Colorado, 1999, pp 14-25.

[11] Nella, J., Atcheson, P., Atkinson, C., Au, D., Blair,

M., Bronowich, A., Fitzgerald, D., Heidenga, J., Lightsey, P., Kelly, T., Matthews, G., Pohner, J., Reynolds, P., Shuchstes, D, Texter, S., Waldie, D., Whitley, R., "Next Generation Space Telescope Observatory Architecture and Performance", Proceedings of the SPIE 4850-26, 1999.

[12] De Weck, O. L., Miller, D. W., and Mosier, G. E., "Multidisciplinary Analysis of the NEXUS Precursor Space Telescope", Proceedings of the SPIE, Volume 4849, pp. 294-304 2002.

[13] Agrawal, B. and Kubby, J., "Applications of MEMS in Segmented Mirror Space Telescopes", Proceedings of the SPIE, Vol. 7931, 793102, 2011, doi:10.1117/12.876503.

[14] Wlodarczyk, K. L., Bryce, E., Schwartz N., Strachan, M., Hutson, D., Maier, R. R. J., Atkinson, D. Beard, S., Baillie, T., Parr Burman, P., Kirk, K., and Hand, D. P., "Scalable Stacked Array Piezoelectric Deformable Mirror for Astronomay and Laser Processing Applications", Review of Scientific Instruments, Vol.85, 024502, 2014,

[15] Champagne, J. A., Crowther, B. G., Newswander, T. T., "Deployable Mirror For Enhanced Imagery Suitable for Small Satellite Applications", 27th Annual AIAA/USU Conference on Small Satellites, SSC13-III-1, 2013, pp 1-9.

[16] Patterson, K., Yamamoto, N., and Pellegrino, S., "Thin Deformable Mirrors for a Reconfigurable Space Telescope", 53rd AIAA/ASME/ASCE/AHS/ASC Structures, Structural Dynamics, and Materials Conference, 2012, pp 1-13.

[17] Somov, Y. I., Butyin, S. A., Matrosov, V. M., Anshakov, G. P., Antonov, Y. G., Makarov, V. P., Sorokin, A. V., Bashkeyev, N. I., and Kondrat' Yev, O. A., "Ultra-precision Attitude Control of a Large Low-orbital Space Telescope", Control Engineering Practice, Vol. 7, 1999, pp 1127-1142.

[18] Dougherty, H., Tompetrini, K., Levinthal, J., and Nurre, G., "Space Telescope Pointing Control System", Journal of Guidance Dynamic and Control, Vol. 5, No. 4, 1982, pp 403-409.

[19] Chubb, W. B., Schultz, D. N., and Seltzer, S. M., "Attitude Control and Precision Pointing of Apollo Telescope Mount", Journal of Spacecraft and Rocket, Vol.5, No. 8, 1968, pp 896-903.

[20] Shimizu, T., Nagata, S., Tsuneta, S., Tarbell, T., Edwards, C., Shine, R., Hoffmann, C., Thomas, E., Sour, S., Rehse, R., Ito, O., Kashiwagi, Y., Tabata, M., Kodeki, K., Nagase, M., Matsuzaki, K., Kobayashi, K., Ichimoto, K., Suematsu, Y., "Image Stabilization System for Hinode Solar Optical Telescope", Solar Physics, 2008, Vol. 249, pp 221-232.

[21] Cheng, J. C. T., Lifshits, J., Grant, C. C., Barbu, M., Zee, R. E., "The BRITE Constellation Space Telescope Design and Test of a Wide Field, High Resolution, Low Noise Optical Telescope for a Nanosatellite Constellation", 25th Annual AIAA/USU Conference on Small Satellite, SSC-11-i-1, 2011, pp 1-20.

[22] Soken, H. E. and Hajiyev, C., "UKF-Based Reconfigurable Attitude Parameters Estimation and Magnetometer Calibration",

IEEE Transactions on Aerospace and Electronic Systems, Vol. 48, No. 3, 2012, pp 2614-2627, doi: 10.1109/TAES.2012.6237612.

[23] Vallado, D. and Finkleman, D., "A Critical Assessment of Satellite Drag and Atmospheric Density Modeling", Acta Astronautica, Vol. 95, 2013, pp 141-165.

[24] Koppenwallner, G., "Satellite Aerodynamics and Determination of Thermospheric Density and Wind", 27th International Symposium on Rarefied Gas Dynamics, 2010, AIP Conference Proceedings 1333, pp 1307-1312, doi: 10.1063/1.3562824.

[25] Titov, E., Burt, J., and Josyula, E., "Satellite Drag Uncertainties Associated with Atmospheric Parameter Variations at Low Earth Orbits", Journal of Spacecraft and Rockets, Vol. 51, No. 3, 2014, pp. 884-892, doi: 10.2514/1.A32686

[26] Pong, C. M., Smith, M. W., Knutson, M. W., Lim, S. Y., Miller, D. W., Seager, S., Villasenor, J. S., and Murphy, S. D., "One Arcsecond Line of Sight Pointing Control on Exlplanetsat A Three Unit CubeSat", Proceedings of the 34th AAS Guidance and Control Conference, Breckenridge, CO, USA, Feb. 4-9, 2011, AAS 11-035, 2011, pp 1-20.

[27] Choi, Y. H. and Bang, H. C., "Dynamic Control Allocation for Shaping Spacecraft Attitude Control Command", KASP International Journal, Vol. 8, No. 1, 2007, pp 10-20.

[28] Patterson, K., "Lightweight Deformable Mirrors for Future Space Telescopes", PhD Dissertation, California Institute of Technology, 2014, pp 1-126.

[29] Hemmati, S., Shahari M., Malekadeh, K., "Active Vibration Control of Satellie Flexible Structures during Attitude Maneuvers", Journal of Applied Sciences, Engineering and Technology, Vol. 5, No. 15, 2013, pp 4029-4037.

[30] Moheimani, R. and Fleming, A. J., "Piezoelectric Transducers for Vibration Control and Damping", Springer, Newcastle, 2005.

[31] Winthrop,M. F. and Cobb, G. B., "Survey of State-of-the-art Vibration Isolation Research and Technology for Space Applications", Proc. SPIE 5052, Smart Structures and Materials 2003: Damping and Isolation, San Diego, California, USA, 2003, pp 13-26.

[32] Singh, T. and Vadali, S. R., "Input Shaped Control of Three Dimensional Maneuvers of Flexible Spacecraft", Journal of Guidance, Control, and Dynamics, Vol. 16, No. 6, 1993, pp. 1061-1068.

[33] Maganti, G. B. and Singh, S. N., "Simplified Adaptive Control of an Orbiting Flexible Spacecraft", Acta Astronautica, Vol. 61, 2007, pp 575-589.

[34] Li, J. Q., Post, M., and Lee, R., "Real-Time Nonlinear Attitude Control System for Nanosatellite Applications", Journal of Guidance, Control, and Dynamics, Vol. 36, No. 6, 2013, pp. 1661-1671, doi: 10.2514/1.59023.